JLB JOURNAL OF LEUKOCYTE BIOLOGY

Check for updates

HIGHLIGHTED ARTICLE

Frontline Science: Dynamic cellular and subcellular features of migrating leukocytes revealed by in vivo lattice lightsheet microscopy

Harriet R. Manley[1] | David L. Potter[2] | John M. Heddleston[3] | Teng-Leong Chew[3] |
M. Cristina Keightley[1,4] | Graham J. Lieschke[1] iD

[1]Australian Regenerative Medicine Institute, Monash University, Clayton, Victoria, Australia

[2]Monash Micro Imaging, Monash University, Clayton, Victoria, Australia

[3]Advanced Imaging Center, HHMI Janelia Research Campus, Ashburn, Virginia, USA

[4]Current address: Department of Pharmacy and Biomedical Sciences, Latrobe Institute of Molecular Sciences, Latrobe University, Bendigo, Victoria, Australia

Correspondence
Graham J. Lieschke, Australian Regenerative Medicine Institute, Monash University, Victoria 3800, Australia.
Email: graham.lieschke@monash.edu

Abstract

Neutrophil and macrophage (Mϕ) migration underpin the inflammatory response. However, the fast velocity, multidirectional instantaneous movement, and plastic, ever-changing shape of phagocytes confound high-resolution intravital imaging. Lattice lightsheet microscopy (LLSM) captures highly dynamic cell morphology at exceptional spatiotemporal resolution. We demonstrate the first extensive application of LLSM to leukocytes in vivo, utilizing optically transparent zebrafish, leukocyte-specific reporter lines that highlighted subcellular structure, and a wounding assay for leukocyte migration. LLSM revealed details of migrating leukocyte morphology, and permitted intricate, volumetric interrogation of highly dynamic activities within their native physiological setting. Very thin, recurrent uropod extensions must now be considered a characteristic feature of migrating neutrophils. LLSM resolved trailing uropod extensions, demonstrating their surprising length, and permitting quantitative assessment of cytoskeletal contributions to their evanescent form. Imaging leukocytes in blood vessel microenvironments at LLSM's spatiotemporal resolution displayed blood-flow-induced neutrophil dynamics and demonstrated unexpected leukocyte-endothelial interactions such as leukocyte-induced endothelial deformation against the intravascular pressure. LLSM of phagocytosis and cell death provided subcellular insights and uncovered novel behaviors. Collectively, we provide high-resolution LLSM examples of leukocyte structures (filopodia lamellipodia, uropod extensions, vesicles), and activities (interstitial and intravascular migration, leukocyte rolling, phagocytosis, cell death, and cytoplasmic ballooning). Application of LLSM to intravital leukocyte imaging sets the stage for transformative studies into the cellular and subcellular complexities of phagocyte biology.

KEYWORDS
lattice lightsheet microscopy, leukocytes, migration, phagocytes, uropod, zebrafish

1 | INTRODUCTION

Neutrophil and macrophage (Mϕ) migration characterize the innate immune response. Understanding leukocyte morphology and dynamics is imperative for understanding inflammation. Intravital microscopy has contributed insights about leukocyte function including chemotactic factors,[1] reverse neutrophil migration,[2] and neutrophil extracellular traps (NETs).[3] Leukocyte migration is one of the most challenging scenarios for in vivo imaging. It must contend with: amoeboid cells perpetually changing shape; unpredictable migration paths despite an overall directionality; and unconstrained migration volumes. Most problematic, leukocyte velocities can outpace the acquisition speeds of conventional microscopes, causing motion artefacts. Neutrophils can reach >20 μm/min in vivo.[4] Increasing temporal resolution to counter this invariably sacrifices axial resolution, limiting volumetric and subcellular morphological detail. In vitro imaging in synthetic matrices or devices addresses some issues, but sacrifices biological context. Only in

---

vivo imaging captures cells within their native 3-dimensional (3D) tissue architecture; necessary for assessing complex truly physiological cell behavior.[5]

Lattice lightsheet microscopy (LLSM) captures high-resolution, near isovolumetric, near real-time images with minimal phototoxicity.[6,7] LLSM has been used to examine leukocytes in vitro,[6,8,9] but in vivo LLSM of zebrafish leukocytes has been demonstrative only, showing only four cells of unknown leukocyte lineage identity.[7] Zebrafish embryos and larvae are ideal for LLSM due to their optical transparency, small size, and genetic tractability. Zebrafish have proved a valuable model for studying phagocytes,[10] with previous multiphoton and confocal imaging discovering several new behaviors: for example, neutrophil reverse migration,[11] $M\phi$s harvesting endothelial exosomes,[12] and $M\phi$ protrusions positioning pigment cells.[13] Here, we successfully adopt LLSM for migrating zebrafish phagocytes, displaying rapid 4-D dynamics and new, subcellular details. We demonstrate LLSM's vastly superior spatiotemporal resolution of migrating leukocytes and position LLSM as a new benchmark for in vivo leukocyte imaging.

2 | MATERIALS AND METHODS

2.1 | Zebrafish

Adult zebrafish were at FishCore (Monash University) or HHMI Janelia Research Campus Vivarium. Embryos were collected in E3 medium (28°C), and in 0.003% (w/v) 1-phenyl-2-thiourea (Sigma–Aldrich) from ≈8 h post fertilization. Zebrafish were single or compound transgenics on a Tübingen background, marking neutrophil or $M\phi$ cytoplasm, neutrophil membranes, blood vasculature, and the neutrophil nuclear lamina. For transgenes, alleles, in-text shorthands and sources see Supplementary Table 1.

2.2 | Ethics and biosafety

Animal experiments were approved by Monash University's Ethics Committee (MARP/2015/094) and performed under Notifiable Low Risk Dealing (PC2-N46/15). Janelia Research Campus experiments were approved by the Janelia IACUC (17-161).

2.3 | Transgenesis

For an N-terminal *eGFP-lmnB2* fusion, *lmnB2* amplified from 3 days postfertilization (dpf) whole-larvae cDNA was directionally cloned into pEGFP-C1 (Clontech) (Primers, Supplementary Table 2). For transgenesis, Tg(*-8mpx:mCherryCaaX*)[gl30] and Tg(*-8mpx:eGFP-lmnB2*)[gl38] Tol2-flanked constructs driven by ≈8 kb of *mpx* promoter[14] were made by standard Gateway cloning (Invitrogen).[15,16] Tg(*-8mpx:mCherryCaaX*)[gl30] was injected into Tg(*mpx:H2Bcerulean-p2A-mko2CaaX*)[gl29] embryos, though this background transgene was not used. Tg(*-8mpx:eGFP-lmnB2*)[gl38] was injected into Tg(*-8mpx:mCherryCaaX*[gl30];*H2Bcerulean-p2A-mko2CaaX*[gl29]) embryos.

2.4 | Tail injuries

2–3 dpf larvae were injured by standard tail transection made distal to the notochord,[17] reproducibly inducing leukocyte migration to the thinnest tail region. Imaging was from ≈3 h post injury (hpi) onward.[11,18]

2.5 | Drug treatments

2.5 hpi tail-transected 3dpf larvae were transferred into E3 containing inhibitors in 1%DMSO: Y-27632 (ROCKi, 22.5 μM, Abcam), blebbistatin (1 μM, Sigma), nocodazole (2 μM, Sigma). E3+1%DMSO was a vehicle-only control. Imaging was from 3hpi, in ≥3 larvae across ≥3 independent experiments.

2.6 | Vital dyes

For a lipophilic fluorescent dye, larvae were incubated 15 min at room temperature in 40 μM unconjugated BODIPY650/665-X succinimidyl ester (Invitrogen, diluted in E3 from 4 mM DMSO stock) then washed in E3 ≥3 times.

2.7 | Confocal microscopy

Injured, anesthetized larvae were mounted in 1% low-melting point agarose for live confocal microscopy in E3+0.002% tricaine. Laser scanning: Zeiss LSM-710; 20 × 0.8 NA water dipping objective. Forty Z slices, interval 0.7 μm. Excitation/Emission (Ex/Em): 454/507, 502/551, 588/696. Spinning disk: Andor Dragonfly; 40 × 1.15 NA water dipping objective. Thirty-six Z slices, interval 0.7 μm. Ex/Em: 488/525, 561/620.

2.8 | Lattice lightsheet imaging

LLSM used 2 instruments: a 3i prototype LLSM at Monash MicroImaging, Monash University, Australia; and the custom Betzig LLSM[6] at the Advanced Imaging Center (AIC), HHMI Janelia Research Campus, USA. Laser power was regulated via an acousto-optic tunable filter (AOTF) into a 28.6 × 0.7NA 3.74 mm WD water-dipping excitation objective (SpecialOptics). Emissions were collected via CFI Apo LWD 25 × 1.1NA water-dipping objective (Nikon), filtered and captured by one Orca Flash4.0v2 sCMOS camera (Hamamastu) (Lightsheet parameters for apodization, Supplementary Table 3). System operation was controlled by LabView Software. Deconvolution point-spread functions were measured using 200 nm TetraSpeck (Invitrogen #T7280) or FluoSphere (Invitrogen #F8803, F8801, F8807) beads on 5 mm coverslips. Data storage and handling was enabled by the Multi-modal Australian Sciences Imaging and Visualization Environment (MASSIVE).[19]

Injured, anesthetized (E3+0.002% tricaine) larvae were mounted in 1% low-melting point agarose on a standard sample holder customized for larval adhesion. Tail injuries were positioned centrally on the 5 mm coverslip area in the Betzig design.[6] Larvae were imaged in a 28°C water bath containing E3+tricaine, with or without drug treatment.
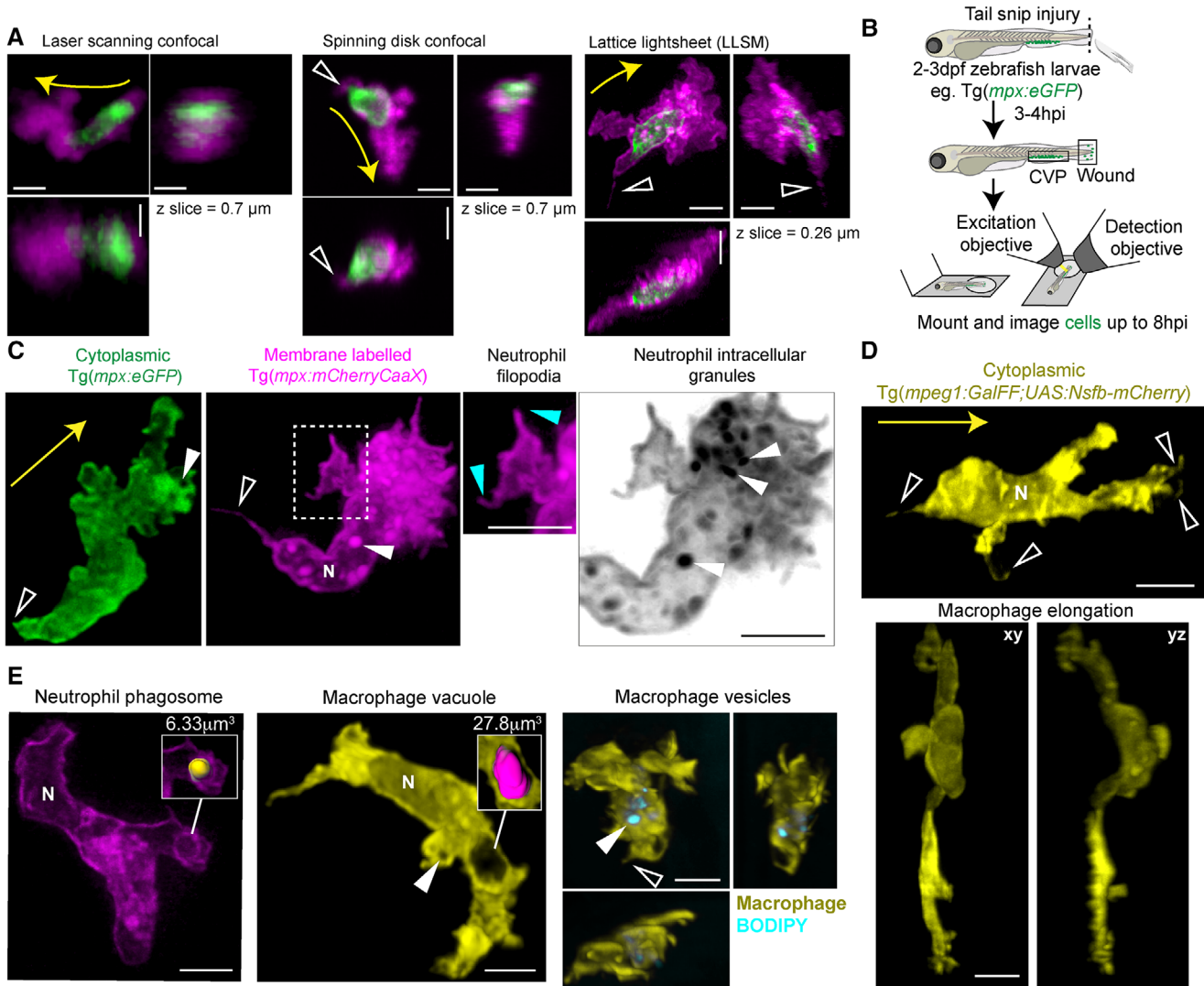
FIGURE 1 Lattice lightsheet microscopy of zebrafish neutrophils and Mφs in vivo. (**A**) Comparison of spatiotemporal resolution for *in vivo* imaging of single migrating neutrophils in the newly generated transgenic line Tg(*mpx:eGFP-lmnB2; mCherryCaaX*) (neutrophil membrane, magenta; nuclear envelope, green). Microscopy: Laser scanning confocal (Zeiss LSM710; 14.7s/Z stack, 256 × 256 cropped, 8-bit), spinning disk confocal (Andor Dragonfly; 37 s/Z stack, 1024 × 1024 cropped, 16-bit), or lattice lightsheet (AIC LLSM; 8.9 s/Z stack, 1024 × 1024 cropped, 16-bit). Z intervals are shown. White arrowheads indicate thin extensions evident in maximum intensity projection and orthogonal sides views, not clearly evident in the lower-resolution confocal microscopy images. (**B**) Schematic for LLSM: lateral mounting of zebrafish tail transection injury model with caudal vein plexus (CVP) and wound imaging sites. (**C**) LLSM of neutrophils with reporter fluorophores either distributed throughout the cytoplasm Tg(*mpx:eGFP*), green, or membrane-localized Tg(*mpx:mCherryCaaX*), magenta, with defined trailing uropod extension (empty arrowhead), filopodia at the leading edge (cyan arrowheads), and intracellular granules (inverted grayscale). Respective image acquisition settings: Time interval: 2 s, Z interval: 0.329 μm, 81 slices (Monash 3i LLSM); Time interval: 8.9 s, Z interval: 0.263 μm, 81 slices (AIC LLSM). (**D**) LLSM of two Mφs with cytoplasmic-distributed reporter fluorophore (Tg(*mpeg1:mCherry*) yellow), one an example of Mφ elongation (with xy and yz views). Respective image acquisition settings: Time interval: 6.1 s, Z interval: 0.263 μm, 121 slices (Monash 3i LLSM); Time interval: 17.8 s, Z interval: 0.140 μm, 201 slices (Monash LLSM). (**E**) LLSM appearance of cytoplasmic vesicles: Tg(*mpx:mCherryCaaX*) neutrophil phagocytic vesicle; Tg(*mpeg1:mCherry*) Mφ vacuole, Tg(*mpeg1:mCherry*) Mφ vesicles labelled with BODIPY lipophilic dye (cyan). Volumetric comparison (μm^3) of the neutrophil phagosome and Mφ vacuole is provided in the inset. Respective image acquisition settings: Time interval: 8.9 s, Z interval: 0.263 μm, 81 slices (AIC LLSM); Time interval: 2.6 s, Z interval: 0.263 μm, 101 slices (Monash LLSM); Time interval: 6.2 s, Z interval 0.263 μm, 121 slices (Monash LLSM).

(Continues)

At Monash, samples were excited by 488 nm (Sapphire LP, Coherent Inc.), 560 nm and 642 nm lasers (MPB Communications) for eGFP, mCherry, and BODIPY650/665-X, respectively. Initial box power was 100–350 mW, AOTF transmittance 0.5–10%. Images acquired with 20–30 ms exposures. Post-image deskewing and deconvo-

lution was run on Monash's MASSIVE HPC cluster using custom Matlab® (vR2017b, Mathworks™) software with 10 iterations of the Richardson-Lucy algorithm (RLA). Single-plane images acquired in Z-stack mode with a piezo interval of 0, no time between stacks and no post-image processing.
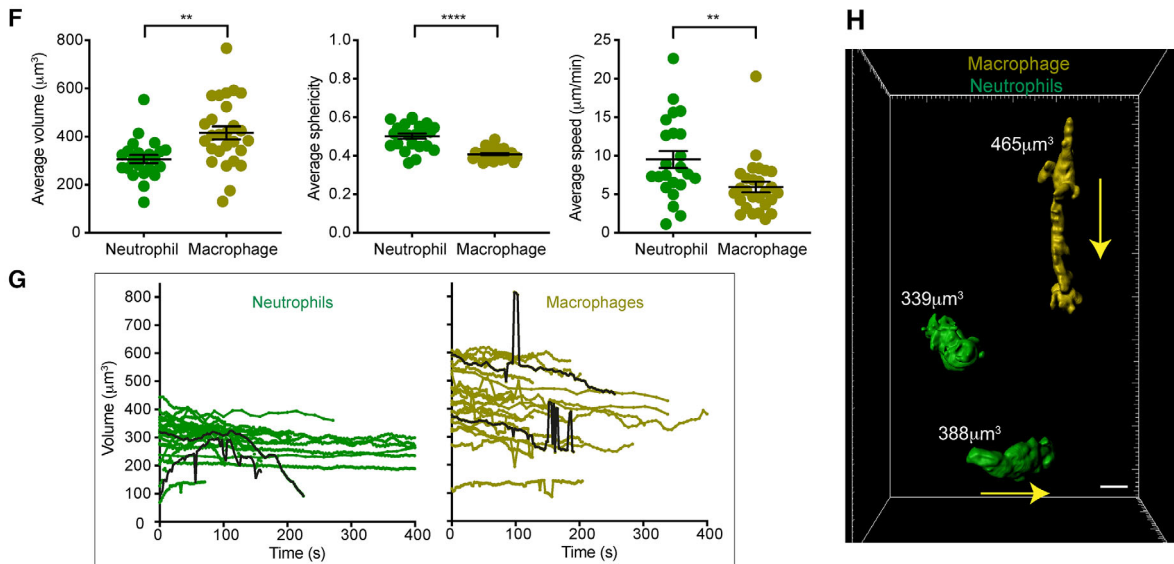
FIGURE 1 (Continued) (**F**) Quantification of Tg(*mpx:eGFP*) neutrophil and Tg(*mpeg1:mCherry*) Mφ volume (306 ± 17 vs. 415 ± 27 µm³), sphericity index (0.52 ± 0.01 vs. 0.41 ± 0.01; where 1 = perfect sphere), and speed (9.5 ± 0.7 vs. 5.9 ± 1.0 µm/min). Datapoints are averages from $n = 23$ neutrophils and $n = 27$ Mφs tracked over time, resulting in 2029 and 1234 temporal datapoints for neutrophils and Mφs, respectively. Unpaired T-tests. $^{**}P < 0.01$, $^{****}P < 0.0001$. (**G**) Quantification of instantaneous Tg(*mpx:eGFP*) neutrophil and Tg(*mpeg1:mCherry*) Mφ volume over time (s) (on average, neutrophils 284 ± 13 µm³ vs. Mφs 399 ± 30 µm³). Each line represents a tracked cell and each dot a measured cell volume. Black lines indicate examples of cells undergoing large shifts in cell volume (>100 µm³). $n = 19$ neutrophils and Mφs, resulting in 1881 and 1257 temporal datapoints for each, respectively. (**H**) Examples of the surface renders used to generate the quantification in (**F**) and (**G**). For all images: refer to Supplementary Video 1. Yellow arrows indicate direction of cell migration, filled white arrowheads indicate cytoplasmic granules, empty white arrowheads indicate thin cytoplasmic extensions, N marks location of nucleus. Maximum intensity projections. Scale bars, 5 µm

At the AIC, Tg(*mpx:eGFP-lmnB2;mCherryCaaX*) larvae were imaged, excited by 488 and 589 nm lasers (MPB Communications) with 100–150 mW initial box power, 75–85% AOTF transmittance. Images acquired with 50 ms exposures. Post-acquisition deskewing and deconvolution used Janelia custom CUDA GPU software run on the Janelia cluster, with 10 iterations of the RLA.

2.9 | Image analysis

Image analyses of deconvolved data used Imaris (Bitplane v9.1.2). Volume and tracking measurements extracted from surface renders generated by background-subtraction contrast thresholding, 0.3 µm smoothing. Intracellular vesicles were manually segmented using the Contour tool. Cytoplasmic extensions were counted manually. Extension length was measured using the Measure tool and defined as distance from the cell body edge to extension tip. Duration was defined as time from extension start (0 µm length) to end (0 µm again). Figures edited in Imaris or Fiji,[20] constructed in Adobe Illustrator (v23.0.2). Orthogonal views scaled proportionally but cropped to region of interest. All other images are maximum intensity projections without re-slicing. Videos generated in Imaris or Fiji, compiled in iMovie (v10.1.9) and HandBrake (v1.2.2).

2.10 | Statistics

Statistics were generated in GraphPad Prism (v8). Error bars are mean ± SEM unless otherwise stated.

2.11 | Data sharing

Original imaging data and deskew-deconvolution codes are available on request.

3 | RESULTS AND DISCUSSION

3.1 | LLSM neutrophil and Mφ morphology in vivo

Migrating zebrafish neutrophil and Mφ morphology has been compared by spinning-disk confocal microscopy, collecting 60 µm³ volumes every 180 s.[21] LLSM substantially improves the spatiotemporal resolution: we routinely acquired 21–31 µm³ volumes with 0.263 µm Z-slices every 4–17 s (Fig. 1A). One-channel Z-stacks achieve even shorter time intervals (≈2 s). Tail transection injuries in 2–3 dpf zebrafish larvae stimulated migration to a restricted, thin anatomical region, preferred for LLSM due to reduced depth and light scattering (Fig. 1B). LLSM resolves fine morphological details of innate zebrafish phagocytes, enabling more accurate quantification of cell speed and volume, and the first assessment of rapid volume changes during leukocyte migration in vivo (Fig. 1; Supplementary Video 1).

Migrating neutrophils carrying the cytoplasmic Tg(*mpx:eGFP*) reporter (Fig. 1C) displayed characteristic polarized amoeboid morphology.[21] Leading-edge pseudopodia were distinct, but lacked defined ruffles or filopodia. At the cell rear, the rounded uropod sometimes displayed small 'knobs', undetected with lower-resolution imaging.[22] Nuclei appeared as large regions of reduced signal intensity.
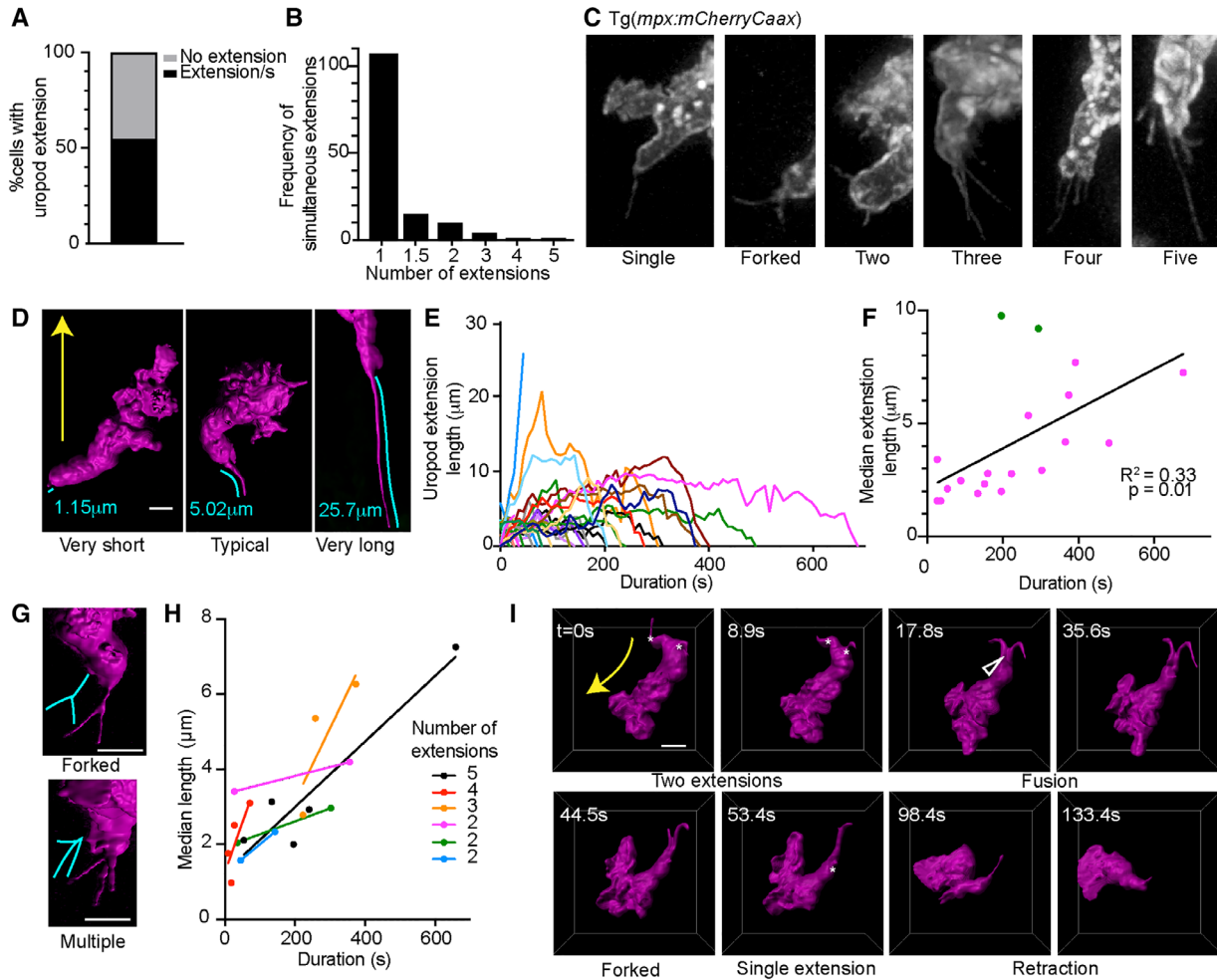
FIGURE 2 Migrating neutrophils commonly carry thin trailing extensions at the uropod. (**A**) Proportion (%) of Tg(*mpx:mCherryCaaX*) neutrophils carrying uropod extensions in injured 2–3 dpf larvae. *n* = 164 cells from 29 datasets across 5 independent experiments. (**B**) Distribution of number of simultaneous extensions; forked uropod extensions are represented by 1.5 value. *n* = 133 cells, 143 simultaneous extension events, total of 171 distinct extensions, across 92 datasets from 13 independent experiments. (**C**) Representative examples of neutrophil uropods with single, forked, 2, 3, 4, and 5 extensions. (**D**) Surface render examples of extension length variation. (**E**) Individual uropod extensions tracked over time. *n* = 11 cells, 28 extensions. Length (μm): mean 4.8; median 3.8; maximum 25.7; minimum 0.30. Duration (s): mean 215; median 196; maximum 676; minimum 27 (including only 21/28 extensions that were tracked from beginning to end). (**F**) Correlation of median extension length and extension duration. Each data point represents 1 complete extension (19 extensions analyzed). Outliers highlighted in green. Linear regression analysis, R^2 = 0.33, $P < 0.05$. (**G**) Surface render examples of a forked extension compared to multiple extensions emanating from the same point on the uropod. (**H**) Plotting the median length of each individual extension when multiple extensions are simultaneously produced from the same uropod over time. Each point represents an individual extension. Randomly-selected examples of cases with 2, 3, 4, and 5 multiple extensions are plotted. Trend lines demonstrate the persistence of the extension with the longest median length. (**I**) Surface render timelapse depicting 2 uropod extensions (marked by asterisks) coming together at a fork (arrowhead) and fusing into a single extension that is then retracted (1 of four examples). Time interval: 8.9 s. Z interval: 0.263 μm, 81 slices (AIC LLSM).

(Continues)

From their size and correlation with other reporters (see below), we interpret the smaller, signal-devoid structures as granules.

Membrane-labeled Tg(*mpx:mCherryCaaX*) neutrophils (Fig. 1C) provided detail of fine membrane structures. Leading-edge pseudopodia displayed tapering filopodia. Uropod "knobs" were revealed as the beginnings of long, thin trailing extensions that underwent dynamic retraction. Multiple ≈0.5–1 μm brightly labeled cytoplasmic spheres represent membrane-lined neutrophilic granules.[17,23] Large fluorophore-absent voids represent nuclear position. Smaller, circular voids were interpreted as phagocytic vesicles due to their size (≈6 μm³) (Fig. 1E) and visual evidence of their formation by phagocytosis.

Differing from neutrophils, cytoplasmic-labeled Tg(*mpeg:mCherry*) Mϕs had more branched morphology, and less-defined front/rear polarization, consistent with more mesenchymal migration (Fig. 1D).[24] Mϕs displayed thin cytoplasmic extensions, elongation, and cytoplasmic voids consistent with the nucleus, vesicles, and the phagocytic vacuoles (≈28 μm³) that characterize Mϕ cytoplasm (Fig. 1E).[9]
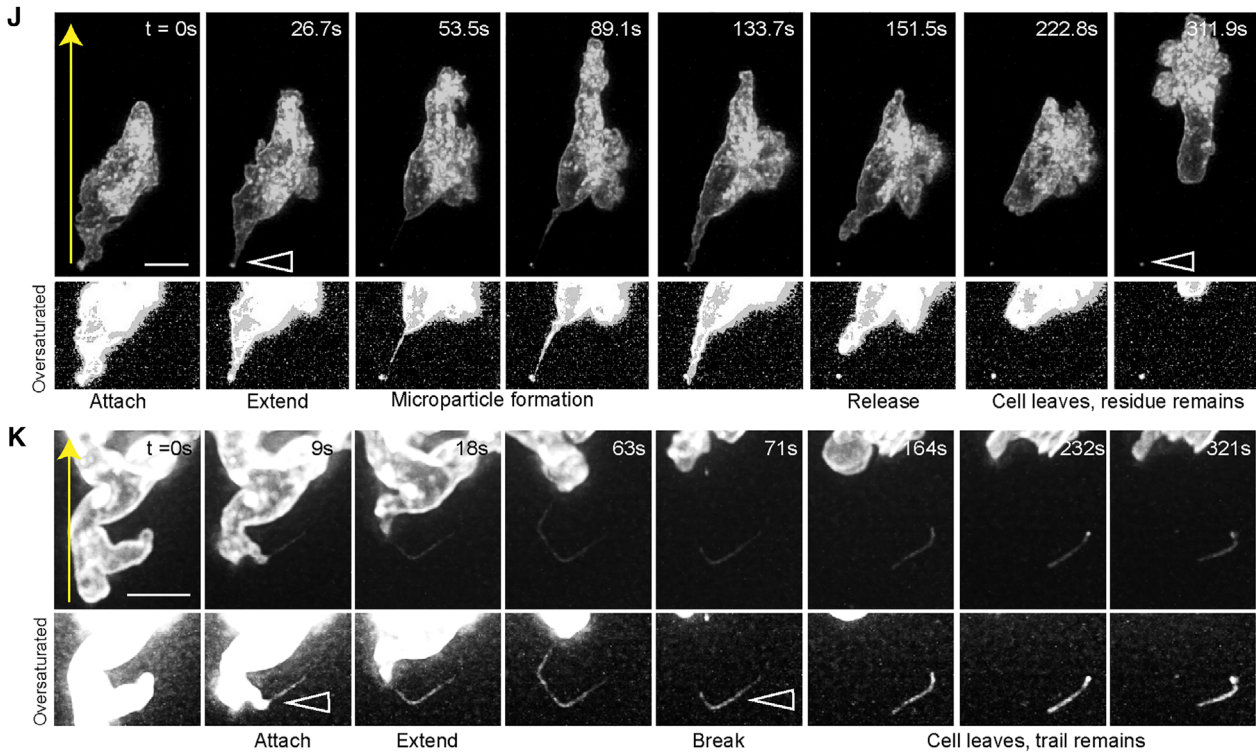
FIGURE 2 (Continued) (**J**) Trailing uropod extension deposits small membrane residue as cell migrates away. White arrows indicate residue at beginning of deposition, and same residue remaining as the cell leaves field of view. Maximum intensity projection (MIP), with oversaturated detail below. Time interval = 4.45 s. Z interval: 0.263 μm, 81 slices (AIC LLSM). (**K**) Uropod extension leaves behind a membrane trail fragment as neutrophil migrates away. White arrows indicate uropod extension forming as rear of cell attaches to substratum, extending, then part of the extension breaking off and remaining as the cell leaves field of view. MIP, with oversaturated detail below. Time interval: 8.91 s. Z interval: 0.263 μm, 81 slices (AIC LLSM). For all images: refer to Supplementary Video 2. Yellow arrows indicate direction of cell migration. Scale bars: 5 μm

LLSM permitted precise, instantaneous volumetric quantification (Fig. 1F–H). As expected, neutrophils migrated faster than Mϕs (9.5 ± 0.7 vs. 5.9 ± 1.0 μm/min), with 35% of neutrophils >12 μm/min. Neutrophils were 26% smaller than Mϕs (306 ± 17 vs. 415 ± 27 μm³), with rounder, less eccentric shape. We also assessed if migrating neutrophils and Mϕs maintained their volume over time (Fig. 1G). Past studies have shown neutrophil volume expands during migration.[25] With LLSM, we found neutrophils remained essentially isovolumetric during migration (284 ± 13 μm³). Per cell, 68% of neutrophil volumes fell within ±13.2% of the cellular mean. However, some neutrophils demonstrated rapid reduction or expansion: one increased from ≈130 to 230 μm³ in <60 s, another shrunk from ≈320 to ≈80 μm³ in <2 min. Mϕs displayed greater absolute volumetric size and variation (399 ± 30 μm³), and underwent relatively large changes in cell volume (>±100 μm³) more often than neutrophils, reflecting more dynamic cell size. Per cell, 68% of Mϕ volumes fell within ±7.5% of the cellular mean. On review, larger volume changes could not be attributed to imaging artefacts or cellular fragmentation.

3.2 | Interstitial migrating neutrophils commonly display dynamic uropod extensions

To explore the utility of LLSM for imaging fine structures of rapidly migrating neutrophils, we focused on uropod extensions; thin, evanes-cent trails poorly visualized by lower-resolution live microscopy.[26,27] From LLSM datasets, we measured their incidence, precise length, duration, and followed their fate (Fig. 2; Supplementary Video 2). LLSM revealed that uropod extensions were present in 54.9% of neutrophils undergoing interstitial migration (Fig. 2A). 76.2% of extensions were singular, but uropods could simultaneously carry up to 5 discrete extensions (Fig. 2B and C). Their average length was 4.6 μm, but could extend to 25.7 μm (Fig. 2D and E). Extensions lasted for 3.21 min (median) but ranged from 26.7 s to 11.27 min (Fig. 2E). While length and persistence were correlated (Fig. 2F), outlier values indicate other factors must impact retraction dynamics. When multiple extensions existed, the longest extension persisted (Fig. 2G and H). Forked extensions represent an intermediate in the coalescence of 2 extensions that, as they retract from different points on the uropod, progressively fuse before retracting as one (Fig. 2I). The dynamics of multiple and forked uropod extensions document a clear disposition toward consolidating into one trailing extension that retracts last.

Some migrating neutrophils left behind a small deposit of neutrophil membrane or a longer thread of extension (Fig. 2J and K). Less than 0.5-μm residues resemble integrin-rich microparticles deposited during uropod detachment.[26] Linear fragments resemble the neutrophil trails that recruit immune cells during infection.[27] But what determines residue deposition, and how do these uropod remnants impact
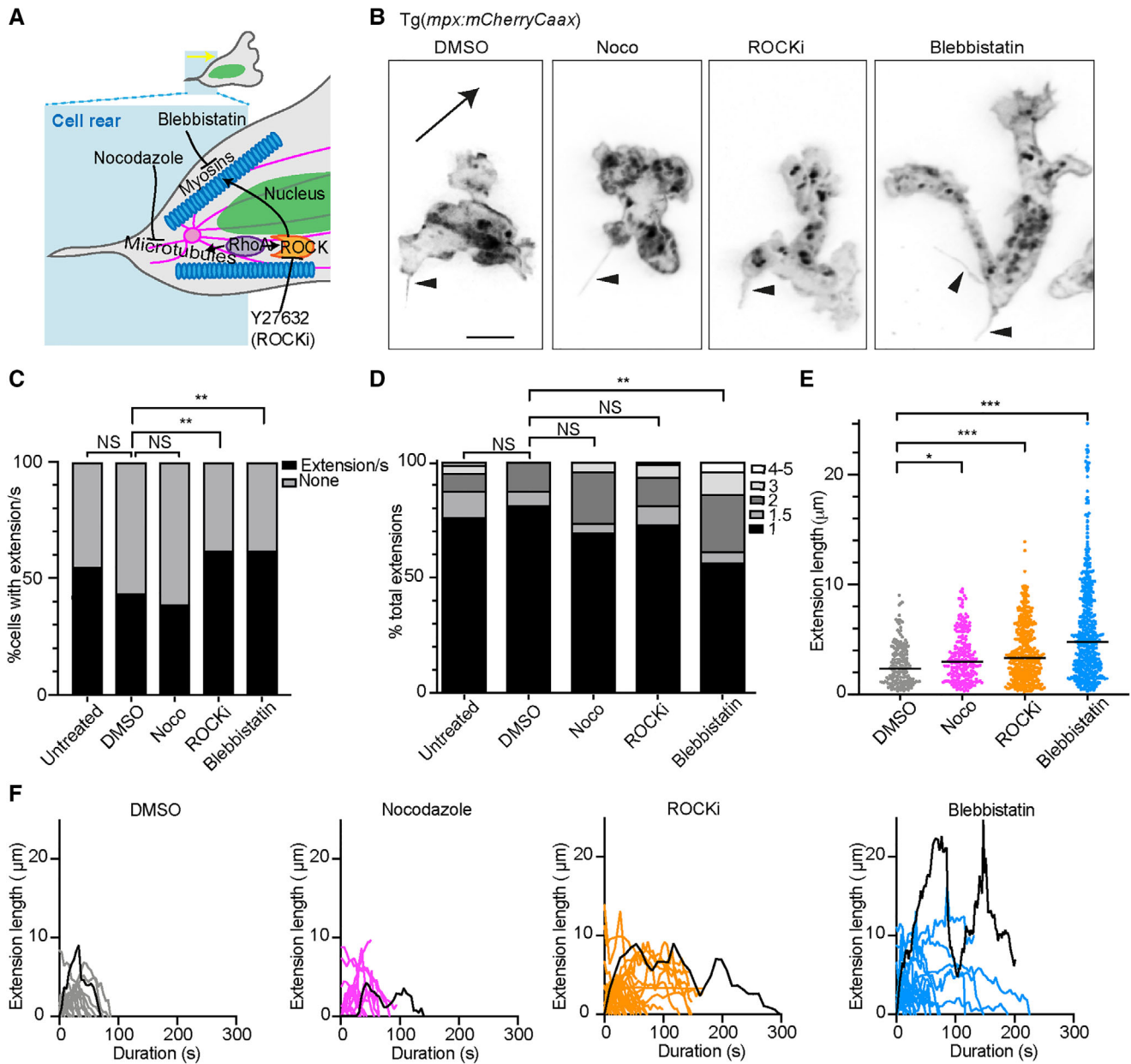
FIGURE 3 **Myosin-II-mediated rear contractility impacts uropod extension dynamics.** (**A**) Schematic diagram of key cytoskeletal components in the uropod: myosins like myosin II (blue), microtubules (pink) and RhoA kinase (ROCK, orange). Drug treatments to target these components: blebbistatin, nocodazole (Noco), and Y-27632 (ROCKi) respectively. (**B**) Uropod extensions in Tg(*mpx:mCherryCaaX*) neutrophils under various drug treatment conditions (Supplementary Video 3). Black arrowheads indicate uropod extensions. Black arrow represents direction of cell migration. Scale bar 5 μm. (**C**) Percentage of cells with uropod extensions. Cells analyzed: untreated $n = 164$, DMSO $n = 27$, Noco $n = 64$, ROCKi $n = 92$, Blebbistatin n = 131. Pairwise Chi-squared tests with Bonferroni correction for multiple comparisons. $^{**}P < 0.01$. (**D**) Relative frequency of multiple simultaneous extensions. Extensions categorized as 1, 1.5 (representing forked extensions), 2, 3, 4 to 5. Cells analyzed: untreated $n = 133$, DMSO $n = 12$, Noco $n = 25$, ROCKi $n = 58$, Blebbistatin $n = 81$. Pairwise Chi-squared tests with Bonferroni correction for multiple comparisons. $^{**}P < 0.01$. (**E**) Instantaneous uropod extension length, plotting all instantaneous values. Extensions analyzed: DMSO 19, Noco 15, ROCKi 31, Blebbistatin 25. Total timepoints: DMSO 186, Noco 281, ROCKi 448, Blebbistatin 530. Cells analyzed: DMSO 11, Noco 7, ROCKi 13, Blebbistatin 7. Kruskal-Wallis test, P-values: $^* < 0.05$, $^{**} < 0.01$, $^{***} < 0.001$. Median length (μm) marked as black line: DMSO 2.40, Noco 3.00, ROCKi 3.37, Blebbistatin 4.82. (**F**) Length uropod extensions from (**E**) plotted against time. Each line represents a tracked extension. Black lines highlight examples of multiple prolongations.
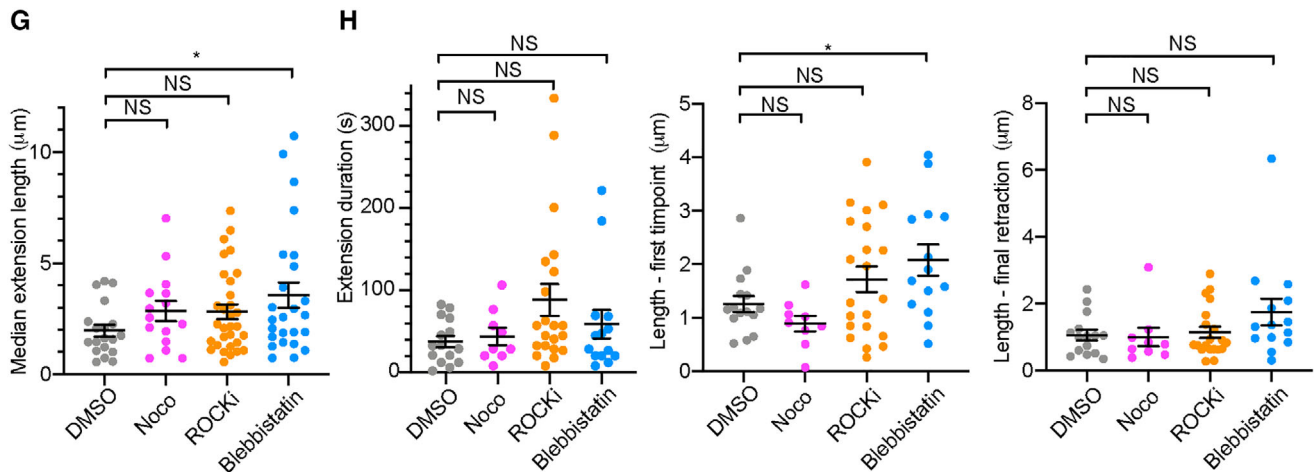
(Continues)

FIGURE 3 (Continued) (**G**) Median length of extensions analyzed in (**E**) and (**F**). Mean length (μm): DMSO 2.7 ± 0.13, Noco 3.4 ± 0.14, ROCKi 3.85 ± 0.12, Blebbistatin 5.90 ± 0.20. * p < 0.05. One-way ANOVA, Dunnett's multiple comparison test. (**H**) Considering only extensions tracked completely from beginning to end, extension duration, extension length at first timepoint, and extension length immediately prior to final retraction (the last timepoint before length = 0 μm). Mean length at last timepoint/final retraction (μm): DMSO 1.06 ± 0.16, Noco 1.00 ± 0.28, ROCKi 1.14 ± 0.17, Blebbistatin 1.75 ± 0.40. Extensions analyzed: DMSO 15, Noco 9, ROCKi 21, Blebbistatin 14. *$P < 0.05$. One-way ANOVA, Dunnett's multiple comparison test. For all analyses: refer to Supplementary Video 2. Images captured of neutrophils in Tg(*mpx: eGFP-lmnB2;mCherryCaaX*) larvae, from 2 (DMSO) or 3 (drug treatments) independent imaging experiments. Time interval: 2.0 or 4.2 s, dependent on 1- or 2-channel acquisition, respectively. Z interval: 0.263 μm, 81 slices (Monash 3i LLSM)

inflammation? LLSM of uropod extension dynamics provides a substantially improved morphological basis for considering their function,[22] and leukocyte biology must from now on factor in these prevalent, long cytoplasmic processes.

3.3 | Myosin II inhibition alters uropod extension dynamics and detachment

Being able to reliably and precisely visualize and measure structures such as uropod extensions permits their determinants to be studied afresh. By perturbing uropod components,[22,28] we evaluated their contribution to extension dynamics (Fig. 3; Supplementary Video 2) and demonstrate reliable, quantifiable endpoints for future studies. Larvae were treated with inhibitors targeting rear cell polarity contributors: microtubules (nocodazole), Rho-associated kinase (Y-7632, ROCKi), and myosin-II (blebbistatin) (Fig. 3A). Nocodazole-treated neutrophils had rounder cell bodies and pseudopodia,[21] but this did not affect uropod extension incidence or number (Fig. 3B–D). Blebbistatin and ROCKi induced neutrophil branching and elongation,[28,29] and ≈20% more rear extensions (Fig. 3C). Blebbistatin-treated cells were also ≈25% more likely to carry multiple or forked extensions (Fig. 3D).

All inhibitors increased representation of time points with longer extensions (Fig. 3E), and saw extensions that extended and retracted numerous times (Fig. 3F), a back-and-forth pattern likely representing failed attempts to detach. Yet on a per cell basis, only myosin-II inhibition saw significantly longer extensions (Fig. 3G) and a significant detachment defect, evident as increased length at the first timepoint (Fig. 3H). As blebbistatin induces more total, multiple and forked extensions from lingering attachments, the consolidation of uropod

extensions retracting from several attachment points involves myosin-II. These in vivo data extend previous in vitro data implicating myosin-II in uropod detachment.[28]

3.4 | LLSM of vascular neutrophils highlights the consequences of adhesion and flow

To assess neutrophil morphology in other microenvironments, we applied LLSM to intra- and peri-vascular neutrophils of the caudal vein plexus (Fig. 4; Supplementary Video 3). Blood flow, shear stress, and endothelial adhesion impact neutrophil migration mode and morphology. Extravascular neutrophils stationed near vessels were nonpolarized and generated small cytoplasmic extensions (Fig. 4B). Even with LLSM, neutrophils transiting in the fastest blood flow streams moved too fast for 3D acquisition, appearing as streaks (Fig. 4C and D). Freely circulating neutrophils lacked maintained polarity, displaying irregular shape induced by shear stress and buffeted motion that saw neutrophils occasionally collide with one another (Fig. 4C). Indeed, Rac-2-deficient neutrophils circulate despite lacking migratory capacity or polarization,[30] and neutrophil adhesion is needed to induce neutrophil polarization.[31]

Figure 4D–E depict a neutrophil that suddenly stops rolling, forming a tether fixing it to a second, stationary intravascular neutrophil. Migrating intravascularly, the cell forms sheet-like lamellipodia before nestling beside a blood vessel wall, its lamellipodia moving with the blood flow. The lamellipodia of intravascular migration were distinct from the leading-edge filopodia and pseudopodia of interstitial migrating cells (Fig. 1). In the much slower blood flow of a capillary, a migrating neutrophil assumed the polarized morphology of interstitial cells, producing a retracting uropod extension (Fig. 4F and G). These
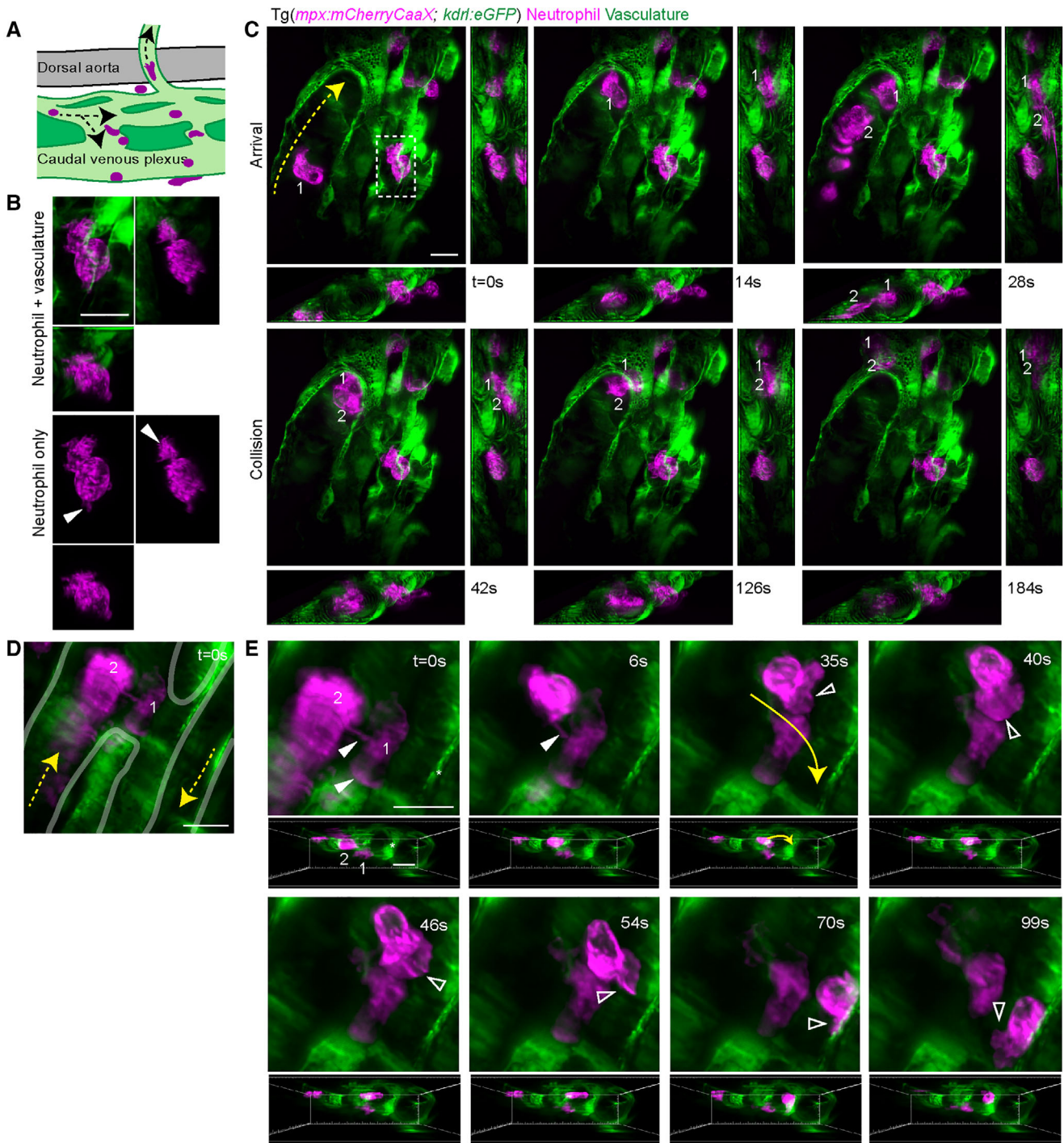
FIGURE 4 **Intravascular and extravascular neutrophil dynamics.** (**A**) Schematic depicting the caudal vein plexus (green) in and around which intra- and extravascular neutrophils (magenta) were imaged by LLSM. Dashed black arrows indicate blood flow. (**B**) Maximum intensity projection (MIP) with orthogonal views of extravascular stationary neutrophil boxed in $t = 0$ panel of (**C**), producing cytoplasmic extensions (white arrowheads). (iii) Appearance of intravascular neutrophils in rapid blood flow in timelapse MIP sequence with orthogonal views. A neutrophil arrives (numbered 1), buffeted through the blood vessel by the blood flow. A second neutrophil (numbered 2) rapidly arrives and collides with the first neutrophil. The two cells become lodged for ≈60 s, before starting to exit the field of view in the final panel. Time interval: 14.48 s. Z interval: 0.158 μm, 201 slices (Monash 3i LLSM). (**D** and **E**) Timelapse MIP sequence of an intravascular neutrophil in rapid flow as it forms a thin tether, stopping near a second neutrophil within the vascular network, and then migrates within the blood vessel. (**D**) Neutrophils marked by numbers, with blood vessel borders outlined. (**E**) White filled arrow shows tether. White empty arrows indicate lamellipodia produced by neutrophil as it migrates within the blood vessel. Below each timepoint is a zoomed-out view that has been rotated on the X-axis clockwise, to orientate each neutrophil (marked by numbers) within the vasculature. An asterisk marks a blood vessel border. Time interval: 5.81 s. Z interval: 0.329 μm, 81 slices (Monash 3i LLSM).
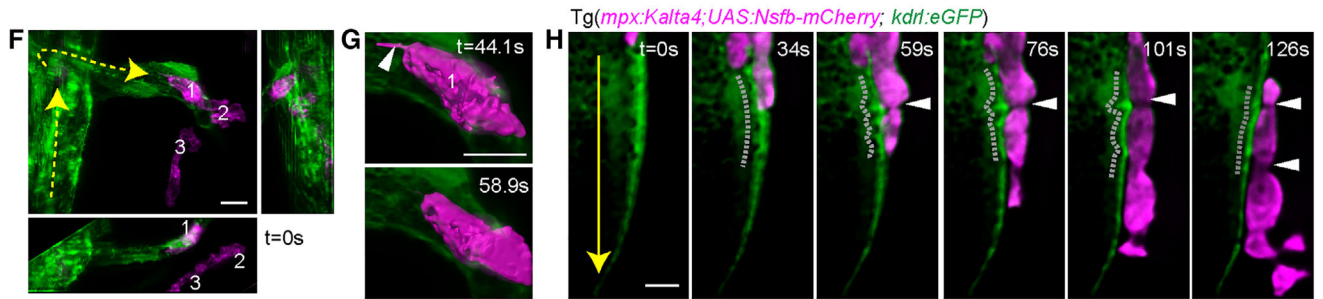
(Continues)

FIGURE 4 (Continued) (**F**) MIP with orthogonal views of a capillary with three neutrophils (1,2,3) present in the field, one of which (1) is within the capillary. (**G**) Surface render demonstrating the uropod extension produced and retracted by the neutrophil as it migrates in the capillary. Time interval: 14.28 s. Z interval: 0.158 μm, 201 slices (Monash 3i LLSM). (**H**) Timelapse MIP sequence of an extravascular neutrophil (magenta) patrolling the outside of a blood vessel (green). Dashed grey lines indicate indentation of the blood vessel by the patrolling neutrophil. White arrows indicate constriction points along cell cytoplasm. Time interval: 4.2 s. Z interval: 0.329 μm, 81 slices (Monash 3i LLSM). For all images: refer to Supplementary Video 3. Yellow dashed arrows indicate blood flow direction, yellow arrows indicate direction of neutrophil migration. Scale bars 10 μm
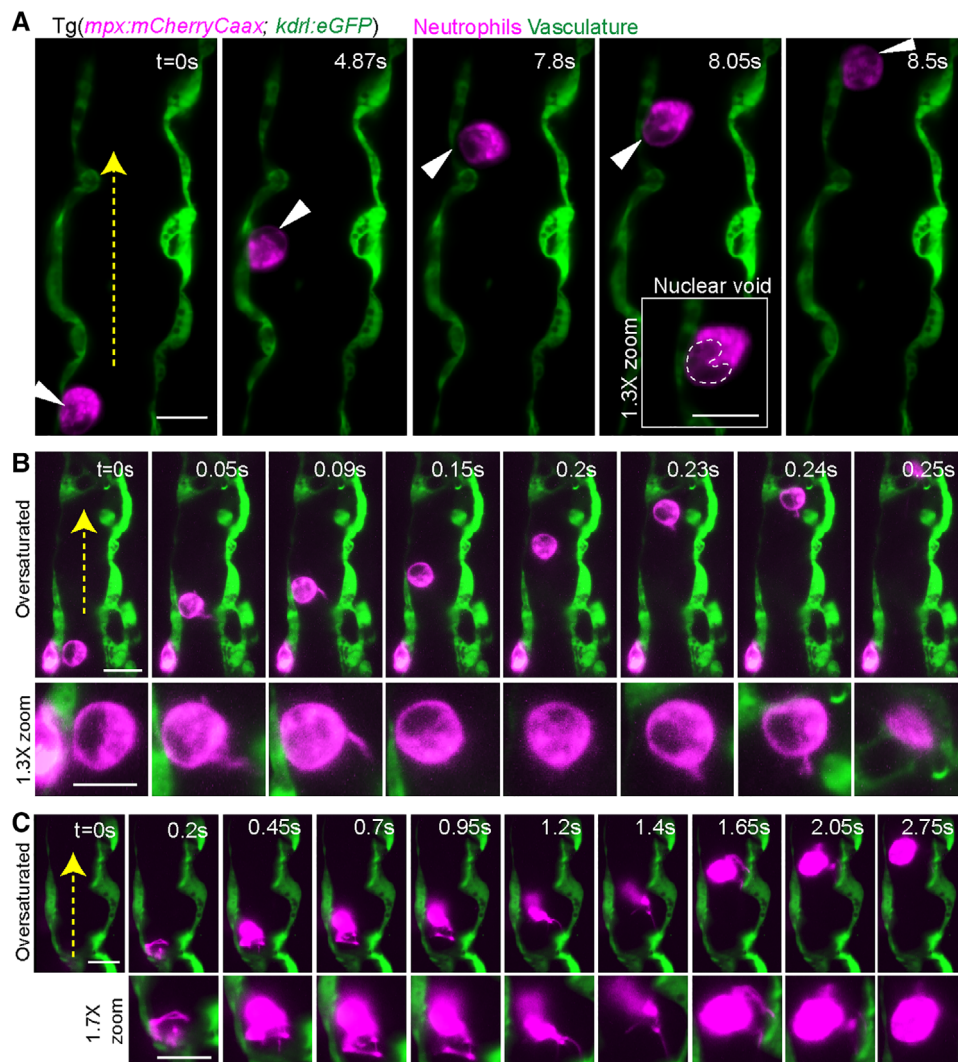

FIGURE 5 **Intravascular rolling neutrophils imaged at very high temporal resolution by single-plane LLSM.** (**A**) Tg(*mpx:mCherryCaaX*) neutrophil (magenta) rolling along the blood vessel endothelium (Tg(*kdrl:eGFP*), green). White arrowhead indicates the nuclear void, also outlined in the inset zoom. (**B**) Example of neutrophil producing short cytoplasmic tethers whilst rolling. Image of cell body oversaturated to show relatively fluorophore-poor tether. (**C**) Example of neutrophil producing long cytoplasmic sling while rolling. For all images: refer to Supplementary Video 3. Yellow dashed arrows indicate blood flow direction; scale bars 10 μm. Images acquired every 50 ms, single-plane imaging with no Z-depth (Monash 3i LLSM). Images of tethers and slings have cell body oversaturated to accentuate relatively fluorophore-poor cytoplasmic extensions
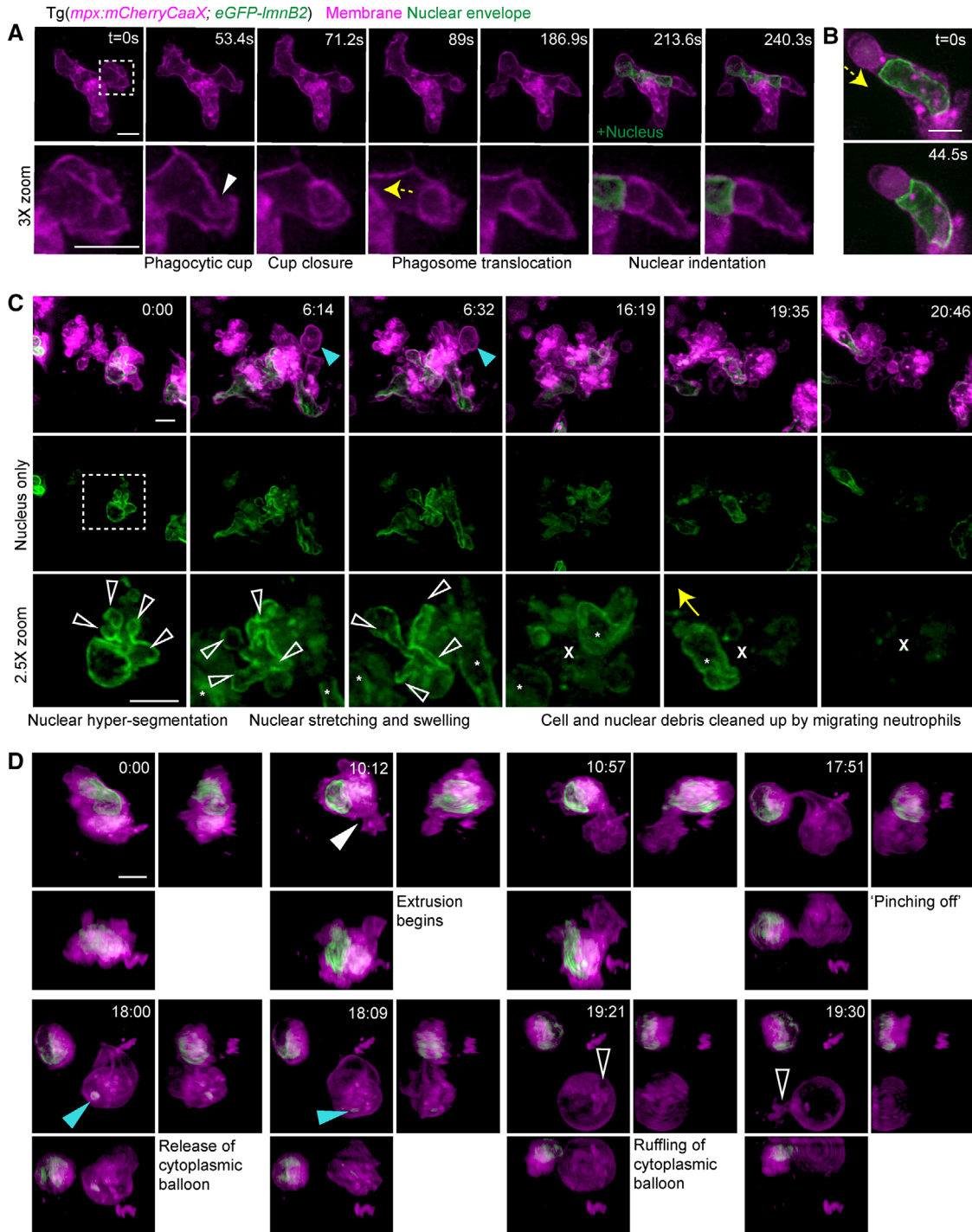
FIGURE 6 **Subcellular neutrophil behaviors imaged with high resolution in vivo.** Imaging series of subcellular neutrophil behaviors captured in the new dual reporter line Tg(*mpx:eGFP-lmnB2; mCherryCaaX*) (labels nuclear envelope, green; neutrophil membranes, magenta). (**A**) Maximum intensity projection (MIP) timelapse series of same cell from Fig. 1E undergoing phagocytosis. White arrowhead indicates invagination forming the phagocytic cup that seals to form a phagosome. The phagosome translocates along the pseudopod (direction indicated by yellow arrow) abuts the nucleus and proceeds to indent the nuclear envelope. (**B**) Second example of phagosome translocation (direction indicated by yellow arrow) with indentation of the nuclear envelope. (**C**) Neutrophil cell death. MIP timelapse series of dying neutrophil (boxed in first frame) with hyper-segmented nucleus. White arrows in 2.5× zoom indicate nuclear lobes, which progressively enlarge. A second neutrophil arrives and clears up the cytoplasmic and nuclear debris of the dying cell (its former position is marked in the frames that follow with an X). Cyan arrowhead marks a second example of cytoplasmic ballooning as detailed further in (**D–F**). Timestamp, min:s. (**D**) MIP timelapse series with orthogonal views of single neutrophil extruding and releasing a cytoplasmic balloon. Filled white arrowhead indicates extrusion beginning. Cyan arrowheads indicate nuclear fragments within the extruded balloon. Empty white arrowheads mark balloon ruffles. Timestamp, min:s. One of two examples, each from independent experiments (second example labeled in C).
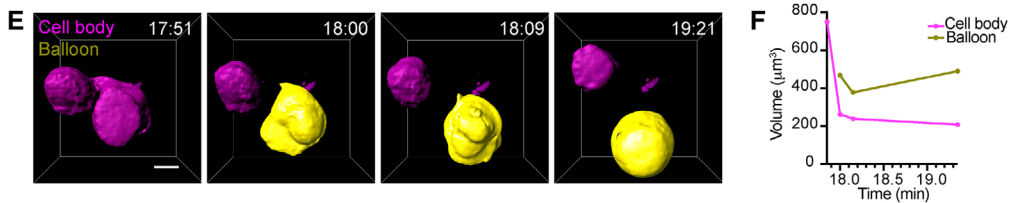
(Continues)

FIGURE 6 (Continued) (**E**) Surface render of selected timepoints from (**D**) showing volumetric difference in cytoplasmic size of cell body (magenta) and balloon (yellow) following balloon extrusion. (**F**) Quantification of cytoplasmic volume (μm^3) over time (elapsed minutes) for cell body and cytoplasmic balloon depicted in (**D**). For all images: refer to Supplementary Video 4. Time interval = 8.9 s. Z interval: 0.263 μm, 81 slices (AIC LLSM). Scale bars, 5 μm

differing morphologies reflect the consequences of the stronger adhesive forces needed to counter blood flow, compared to the weaker adhesion forces of interstitial migration.[32]

3.5 | Neutrophils exert forces distorting endothelial shape

Neutrophils patrolling extravascular tissues adopted polarized morphology similar to neutrophils migrating to a wound, but were often more elongated, with constrictions along their length likely from negotiating dense tissue.[33] One neutrophil sliding along the outside of a blood vessel distorted the endothelium, exerting a compressive force exceeding intravascular blood pressure (Fig. 4H; Supporting Video 3). Extravascular constraints may be causing the neutrophil to press against the more flexible endothelium. Alternatively, this event could represent the neutrophil probing for an endothelial weakness through which to squeeze.

3.6 | High-speed single-plane LLSM of rolling neutrophils displays tethers and slings

To capture faster-rolling intravascular neutrophils, we applied single-plane LLSM, which achieves greater temporal resolution (2 channels, 200 frames/s) at the sacrifice of axial resolution (no Z-depth) (Fig. 5; Supplementary Video 3). Rounded, rolling neutrophils produced, short cytoplasmic tethers or lengthier slings that attached and detached as cells moved along the inner endothelium (Fig. 5B and C). These tethers resembled those described in mouse venules,[34] but were here imaged faster, with labeling of both vessels and neutrophils. We anticipate single-plane LLSM will complement 4-D imaging when examining intravascular behaviors like leukocyte rolling, transmigration, and circulation of extracellular vesicles[12] and thrombocytes.

3.7 | LLSM reveals subcellular insights into neutrophil phagocytosis and cell death

Higher spatiotemporal resolution sets the scene for discovering new cellular behaviors (Supplementary Video 4). Figure 6A displays highly resolved stages of phagosome formation in a membrane-labeled neutrophil: phagocytic cup invagination, closure, and internal budding; phagosome translocation, and ultimately indentation of the flexible nuclear envelope (outlined by Tg(*mpx:eGFP-lmnB2*)). Nuclear indenta-

tion indicates fully-internalized phagosomes can exert localized pressure. Indentation may represent phagosome trafficking and nuclear docking,[35] and is potentially assisted by the closely associated cell membrane that appears to squeeze inwards as phagosomes translocate towards the nucleus (Fig. 6A and B).

Some neutrophils underwent cell death, evidenced by their progressive nuclear fragmentation, immobility, and ultimate removal by incoming neutrophils (Fig. 6C; Supplementary Video 4). Zebrafish neutrophil nuclei are usually bi-lobed,[17] yet the nucleus of the dying cell in Fig. 6C hyper-segments into 4–5 lobes, which distort for ≈8 min before nuclear breakdown (≈16 min). Three of 17 hyper-segmented neutrophils were followed entirely to cell death. We interpret nuclear hyper-segmentation as cell death onset. However, apoptosis and necrosis typically cause neutrophil nuclei to lose their lobes; not segment, swell, and stretch.[36] It is also unlikely to be NETosis, as nuclear rounding precedes NETs.[37] Hyper-segmentation is either a distinct form of cell death, or a further process in cell death or NETosis previously overlooked. These questions, though not answered here, demonstrate that high-resolution LLSM with appropriate reporters for cell death pathways will likely provide new insights.

The neutrophil of Fig. 6D–F extrudes a cytoplasmic "balloon" that takes with it most of the cell's volume (Supplementary Video 4). After pinching off the cell body, it exists for >90 s and ruffles. We interpret cytoplasmic ballooning as a new extreme of blebbing associated with neutrophil fragmentation and cell death,[38] a contributor to neutrophil recruitment and swarming.[4] Yet several features of ballooning are atypical of apoptosis or necrosis: lack of overall cell blebbing or swelling, limited nuclear fragmentation, and the balloon becoming larger than the residual cell.[36,38] Some aspects of ballooning suggest it may represent non-lytic NETs that are released via exocytic vesicles.[39] Ballooning is distinct from vesicular exocytosis, yet the nuclear envelope content and ruffling of balloons are suggestive of large NET-expelling vesicles.[3] Further markers would ascertain which death or NET pathway ballooning represents. By providing the resolution to observe unexpected events, LLSM will expand the repertoire of in vivo leukocyte behaviors. Combining LLSM with specific, subcellular transgenics (e.g., our nuclear envelope reporter) offers enormous potential to re-evaluate the in vivo subcellular dynamics of many leukocyte activities.

Intravital LLSM presents some technical challenges. Factoring the current instruments' dimensions, in vivo LLSM is limited to small model

organisms. Zebrafish larvae are optically accessible and ideal size,[6,7] but larval age and imaging site depth must still be considered for lightsheet design and mounting. Blood flow and refractive variation between tissues can create lightsheet scattering and shadowing artefacts. Without bright-field or differential interference contrast sample scouting is difficult, particularly to find randomly, rapidly mobile leukocytes. Auto-fluorescence and additional markers, transgenes, or dyes, can assist anatomical orientation but may introduce fluorescence crossover and noise. We used first-generation LLSM instruments but newer iterations address some technical limitations. Notably, adaptive optics can improve spatial resolution and capacity to probe deep tissues.[7]

Assessing leukocytes within their 3D in vivo context is imperative to understanding their physiological behavior.[5] The LLSM capabilities we exhibit here open up a previously unattainable world of fast, intricate cellular and subcellular dynamics. For neutrophils, open questions regarding vesicle and organelle dynamics, host-pathogen interactions, tethers, cell death, and NETs will greatly benefit from in vivo LLSM.[40] Adopting LLSM as a mainstream imaging modality will transform our understanding of blood cell biology, setting a new standard for in vivo leukocyte imaging.

ACKNOWLEDGMENTS

AUTHORSHIP

DISCLOSURE

The authors declare no conflict of interest.

ORCID

Graham J. Lieschke ID https://orcid.org/0000-0003-0325-798X

REFERENCES

1. Beerman RW, Matty MA, Au GG, et al. Direct in vivo manipulation and imaging of calcium transients in neutrophils identify a critical role for leading-edge calcium flux. *Cell Rep.* 2015;13:2107-2117.
2. Wang J, Hossain M, Thanabalasuriar A, Gunzer M, Meininger C, Kubes P. Visualizing the function and fate of neutrophils in sterile injury and repair. *Science.* 2017;358:111-116.
3. Yipp BG, Petri B, Salina D, et al. Infection-induced NETosis is a dynamic process involving neutrophil multitasking in vivo. *Nat Med.* 2012;18:1386-1393.
4. Lämmermann T, Afonso PV, Angermann BR, et al. Neutrophil swarms require LTB4 and integrins at sites of cell death in vivo. *Nature.* 2013;498:371-375.
5. te Boekhorst V, Preziosi L, Friedl P. Plasticity of cell migration in vivo and in silico. *Annu Rev Cell Dev Biol.* 2016;32:491-526.
6. Chen BC, Legant WR, Wang K, et al. Lattice light-sheet microscopy: imaging molecules to embryos at high spatiotemporal resolution. *Science.* 2014;346:1257998.
7. Liu T-L, Upadhyayula S, Milkie DE, et al. Observing the cell in its native state: imaging subcellular dynamics in multicellular organisms. *Science.* 2018;360:eaaq1392.
8. Fritz-Laylin LK, Riel-Mehan M, Chen B-C, et al. Actin-based protrusions of migrating neutrophils are intrinsically lamellar and facilitate direction changes. *eLife.* 2017;6:e26990.
9. Condon ND, Heddleston JM, Chew T-L, et al. Macropinosome formation by tent pole ruffling in macrophages. *J Cell Biol.* 2018;217: 3873-3885.
10. Lieschke GJ, Currie PD. Animal models of human disease: zebrafish swim into view. *Nat Rev Genet.* 2007;8:353-367.
11. Robertson AL, Holmes GR, Bojarczuk AN, et al. A zebrafish compound screen reveals modulation of neutrophil reverse migration as an anti-inflammatory mechanism. *Sci Transl Med.* 2014;6:225ra29.
12. Verweij FJ, Revenu C, Arras G, et al. Live tracking of inter-organ communication by endogenous exosomes in vivo. *Dev Cell.* 2019;48:573-589.e4.
13. Eom DS, Parichy DM. A macrophage relay for long-distance signaling during postembryonic tissue remodeling. *Science.* 2017;355: 1317-1320.
14. Mathias JR, Perrin BJ, Liu TX, Kanki J, Look AT, Huttenlocher A. Resolution of inflammation by retrograde chemotaxis of neutrophils in transgenic zebrafish. *J Leukoc Biol.* 2006;80:1281-1288.
15. Kwan KM, Fujimoto E, Grabher C, et al. The Tol2kit: a multisite gateway-based construction kit for Tol2 transposon transgenesis constructs. *Dev Dyn.* 2007;236:3088-3099.
16. Ellett F, Pazhakh V, Pase L, et al. Macrophages protect *Talaromyces marneffei* conidia from myeloperoxidase-dependent neutrophil fungicidal activity during infection establishment in vivo. *PLoS Pathog.* 2018;14:e1007063.
17. Lieschke GJ, Oates AC, Crowhurst MO, Ward AC, Layton JE. Morphologic and functional characterization of granulocytes and macrophages in embryonic and adult zebrafish. *Blood.* 2001;98:3087-3096.
18. Renshaw SA, Loynes CA, Trushell DM, Elworthy S, Ingham PW, Whyte MK. A transgenic zebrafish model of neutrophilic inflammation. *Blood.* 2006;108:3976-3978.

19. Goscinski WJ, McIntosh P, Felzmann U, et al. The multi-modal Australian ScienceS Imaging and Visualization Environment (MASSIVE) high performance computing infrastructure: applications in neuroscience and neuroinformatics research. *Front Neuroinform*. 2014; 8:30.

20. Schindelin J, Arganda-Carreras I, Frise E, et al. Fiji: an open-source platform for biological-image analysis. *Nat Methods*. 2012;9:676.

21. Barros-Becker F, Lam PY, Fisher R, Huttenlocher A. Live imaging reveals distinct modes of neutrophil and macrophage migration within interstitial tissues. *J Cell Sci*. 2017;130:3801-3808.

22. Hind LE, Vincent WJ, Huttenlocher A. Leading from the back: the role of the uropod in neutrophil polarization and migration. *Dev Cell*. 2016;38:161-169.

23. Colucci-Guyon E, Batista AS, Oliveira SD, et al. Ultraspecific live imaging of the dynamics of zebrafish neutrophil granules by a histopermeable fluorogenic benzochalcone probe. *Chem Sci*. 2019;10: 3654-3670.

24. Van Goethem E, Poincloux R, Gauffre F, Maridonneau-Parini I, Le Cabec V. Matrix architecture dictates three-dimensional migration modes of human macrophages: differential involvement of proteases and podosome-like structures. *J Immunol*. 2010;184: 1049-1061.

25. Worthen GS, Henson PM, Rosengren S, Downey GP, Hyde DM. Neutrophils increase volume during migration in vivo and in vitro. *Am J Respir Cell Mol Biol*. 1994;10:1-7.

26. Hyun YM, Sumagin R, Sarangi PP, et al. Uropod elongation is a common final step in leukocyte extravasation through inflamed vessels. *J Exp Med*. 2012;209:1349-1362.

27. Lim K, Hyun Y-M, Lambert-Emo K, et al. Neutrophil trails guide influenza-specific CD8+ T cells in the airways. *Science*. 2015;349:aaa4352.

28. Eddy RJ, Pierini LM, Matsumura F, Maxfield FR. Ca2+-dependent myosin II activation is required for uropod retraction during neutrophil migration. *J Cell Sci*. 2000;113:1287-1298.

29. Jennings RT, Strengert M, Hayes P, et al. RhoA determines disease progression by controlling neutrophil motility and restricting hyperresponsiveness. *Blood*. 2014;123:3635-3645.

30. Deng Q, Yoo SaK, Cavnar PJ, Green JM, Huttenlocher A. Dual roles for *rac2* in neutrophil motility and active retention in zebrafish hematopoietic tissue. *Dev Cell*. 2011;21:735-745.

31. Ren C, Yuan Q, Braun M, et al. Leukocyte cytoskeleton polarization is initiated by plasma membrane curvature from cell attachment. *Dev Cell*. 2019;49:206-219.e7.

32. Lämmermann T, Sixt M. Mechanical modes of 'amoeboid' cell migration. *Curr Opin Cell Biol*. 2009;21:636-644.

33. Wang X, Jodoin E, Jorgensen J, et al. Progressive mechanical confinement of chemotactic neutrophils induces arrest, oscillations, and retrotaxis. *J Leukoc Biol*. 2018;104:1253-1261.

34. Marki A, Buscher K, Mikulski Z, Pries A, Ley K. Rolling neutrophils form tethers and slings under physiologic conditions in vivo. *J Leukoc Biol*. 2018;103:67-70.

35. Keller S, Berghoff K, Kress H. Phagosomal transport depends strongly on phagosome size. *Sci Rep*. 2017;7:17068-17068.

36. Fuchs TA, Abed U, Goosmann C, Hurwitz R, Schulze I, Wahn V. Novel cell death program leads to neutrophil extracellular traps. *J Cell Biol*. 2007;176:231-241.

37. Neubert E, Meyer D, Rocca F, et al. Chromatin swelling drives neutrophil extracellular trap release. *Nat Commun*. 2018;9:3767.

38. Tixeira R, Caruso S, Paone S, et al. Defining the morphologic features and products of cell disassembly during apoptosis. *Apoptosis*. 2017;22:475-477.

39. Castanheira FV, Kubes P. Neutrophils and NETs in modulating acute and chronic inflammation. *Blood*. 2019;133:2178-2185.

40. Ley K, Hoffman HM, Kubes P, et al. Neutrophils: new insights and open questions. *Sci Immunol*. 2018;3:eaat4579.

SUPPORTING INFORMATION

Additional information may be found online in the Supporting Information section at the end of the article.